NUMERICAL SIMULATION AND EXPERIMENTAL INVESTIGATION OF MICROSTRUCTURE EVOLUTION AND FLOW BEHAVIOR IN THE RHEOLOGICAL SQUEEZE CASTING PROCESS OF A356 ALLOY

Wentao Xiong, Yichao Ding, Zhihua Hu, Binghua Jiang, Mengjue Li and Quan Zou
School of Materials and Environmental Engineering, Chengdu Technological University, Chengdu 611730, Sichuan, People's Republic of China

Abstract

This paper carried out numerical simulations of the entire process of rheological squeeze casting of A356 alloy, evaluated the impact of various combinations of forming process parameters on the temperature field, flow field, and solid-phase fraction of A356 semi-solid slurry, and studied the influence of die temperature (°C) and filling speed (mm/s) on the microstructure formation mechanism of A356 alloy rheological squeeze castings. The research revealed that A356 alloy castings with diverse microstructural features can be achieved by solely controlling the rheological squeeze casting process parameters, without the use of additional heterogeneous nucleating agents or heat treatment. Through combined numerical simulation and experimental results, the optimal rheological squeeze casting process parameters were determined: filling speed of 20 mm/s and mold temperature of 350 °C. It was observed that with the simultaneous increase of mold temperature and filling speed, the average equivalent diameter of the α-Al phase significantly increased from 26.18 μm to 44.27 μm, the uniformity of the eutectic structure distribution was greatly improved, and it was also found that the excessively high filling speed is a critical factor contributing to the coexistence of the script-shaped π-Al$_8$FeMg$_3$Si6 phase and the undecomposed the needle-like β-Al$_5$FeSi phase.

Keywords: A356 alloy, semi-solid rheological squeeze casting, liquid-metal instantaneous undercooling, nucleation, flow behavior, microstructure

Introduction

The Al–Si alloy, characterized by its lightweight, good castability, low cost, and excellent comprehensive performance, is widely used in the aerospace, aviation, and automotive industries.[1–3] The microstructure of Al–Si alloy castings is mainly composed of primary α-Al dendrites, interdendritic irregular Al–Si eutectic phases, and other intermetallic phases, whose shapes and distributions often determine the comprehensive performance of the alloy.[4]

The semi-solid processing (SSP) technology, as a metal forming technique, combines the advantages of traditional forging and casting methods.[5] Megalingam et al.[6] found that the semi-solid slurry has good flowability, low filling temperature, stable filling, and fine microstructure, making it suitable for forming processes such as die casting and squeeze casting. Gao et al.[7] believed that the main advantage of the semi-solid slurry lies in its special semi-solid structure. Therefore, the semi-solid processing technology has become an effective method for producing high-quality Al–Si–Mg alloy automotive components, such as steering knuckles and control arms.

Research on semi-solid alloys has utilized a variety of slurry preparation methods. The mainstream methods for preparing semi-solid billets/slurries include: mechanical stirring method,[8] electromagnetic stirring method,[9] cooling slope method,[10,11] forced convection method, etc.[12] Among these methods, the cooling slope method is considered as a simple, reliable, and economically efficient method for preparing a semi-solid slurry, and it effectively refines the microstructure of aluminum alloys and enhances their mechanical properties.[13] When combined with high-

pressure casting or rheological squeeze casting, this method can produce diverse aluminum alloy castings, such as A356, A201, 2618, 6063, and 7075.[14] However, as rheological squeeze casting results in diverse and complex products, it also leads to inevitable defects in diecasting production. Obtaining optimal process parameters solely through experimentation will increase production costs. Therefore, before conducting experiments, it is essential to conduct a reasonable numerical simulation of the experimental process to develop a rational experimental plan. Ren et al.[15] designed an aluminum alloy semi-solid diecasting injection system through numerical simulation and determined the optimal pouring temperature, injection speed, and mold temperature. Similarly, Das et al.[16] studied the temperature, viscosity, speed, and pressure during the filling process of A356 alloy through numerical simulation, determining the best process parameters and discussing the microstructure and properties of semi-solid die-cast aluminum alloy steering knuckles.

Iron (Fe), as a common impurity in Al–Si–Mg alloys, directly reduces the mechanical properties, corrosion resistance, and machinability of the products.[17] Due to the low solid solubility of Fe in solid Al, during the solidification process, Fe easily forms Fe-rich intermetallic compounds such as α-Al_8Fe_2Si, β-Al_5FeSi, and π-$Al_8Mg_3FeSi_6$.[18,19] These hard and brittle intermetallic compounds not only serve as initiation points for cracks but also provide further paths for crack expansion in Al–Si–Mg alloys.[20,21] It has been found that when the Fe content is low, Fe-rich intermetallic compounds tend to form a needle-like morphology of the β-Al_5FeSi phase rather than the α-Al_8Fe_2Si phase.[21,22] Researchers have explored transforming the β-Al_5FeSi phase into other phases or altering its morphology to enhance the alloy's mechanical properties.[23] Gu et al.[24] utilized the Swirled Enthalpy Equilibration Device (SEED) process to prepare A356 alloy semi-solid slurries and subsequently employed a high-pressure die-casting machine to manufacture intricate components. Their study revealed that solid solution treatment can dissolve the π-$Al_8Mg_3FeSi_6$ phase and promote the growth of the β-Al_5FeSi phase. Other researchers have sought to mitigate the impact of the β-Al_5FeSi phase by incorporating rare elements (e.g., La, Ce, Nb, V) into the Al–Si–Mg alloy melt.[25–27] On the one hand, this method does not directly reduce the Fe content, so the effect is not very significant; on the other hand, the addition of rare elements may lead to solute segregation, which is not conducive to maintaining the mechanical properties of the alloy.[21]

According to the above analysis, a predominant focus of current research is on the alloy composition, casting methods, heat treatment methods, and strengthening mechanism of Al–Si series alloy.[28–30] Nevertheless, there is limited research on Fe-rich intermetallic compounds in low-Fe content (< 0.4 wt%) Al–Si–Mg alloys, particularly concerning the evolution of their microstructure in the casting alloys. Moreover, there is even less research on the distribution and morphology of Fe-rich intermetallic compounds in conjunction with the semi-solid rheological squeeze casting forming process. Therefore, it is essential to clarify the potential governing laws of the rheological squeeze casting process of Al–Si–Mg alloys and the Fe-rich intermetallic compounds before developing a new forming process to address the compatibility issues between alloy properties and processability.

This paper utilized a commercial modeling software, Pro-CAST, for simulating and analyzing the rheological squeeze casting process of A356 alloy. Employing an orthogonal experimental design, the study investigated the impact of various forming process parameters on the temperature field, velocity field, and solid-phase fraction during the filling process of A356 alloy. The primary focus was on analyzing the effects of mold temperature (°C) and filling speed (mm/s) on the microstructure of A356 alloy castings, with the aim of preparing A356 alloy thin-walled parts exhibiting enhanced structural uniformity. The microstructure and morphology of these parts were observed, and the evolution mechanism of A356 microstructure, as well as the influence of process parameters on the evolution of Fe-rich intermetallic compound structure, was discussed. Additionally, the phase transformation and morphological changes of Fe-rich intermetallic compounds were summarized.

Materials and Experimental Process

Materials

The A356 alloy rheological squeeze castings investigated in this paper are predominantly utilized as thin rail guides for a specific vehicle. As indicated in Table 1, commercial A356 alloy ingots were utilized, and the chemical composition of the alloy was assessed using a wavelength dispersive X-ray fluorescence spectrometer (AxioSmAX).

Numerical Simulation and Experimental Process of Semi-Solid Rheological Squeeze Casting of A356 Alloy

Finite Element Model

Many studies have demonstrated that the shear stress increases with shear rate until a specific shear state is attained, after which the stress accumulation in the semi-solid melt is primarily dependent on the solid-phase fraction within the matrix.[31,32] Consequently, the solid-phase

Table1. Chemical Composition of A356 Alloy

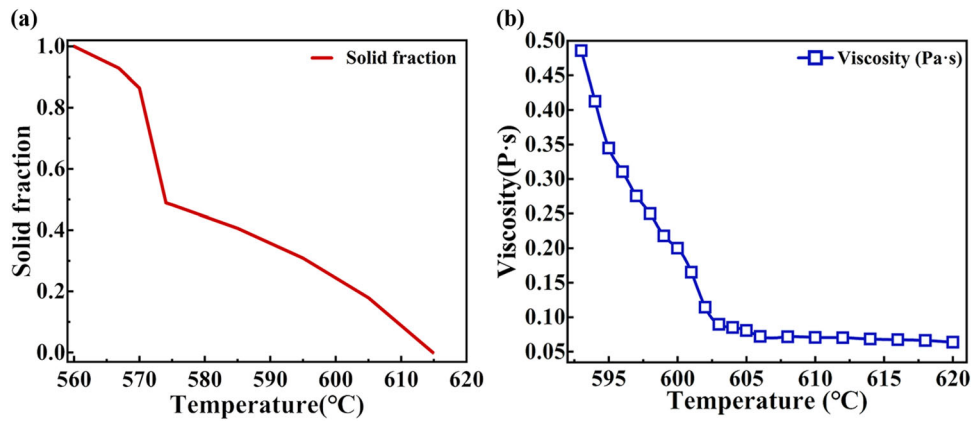| Element	Si	Mg	Fe	Cu	Mn	Ti	Al
Content [wt%]	6.76	0.32	0.11	0.02	0.01	<0.01	Balance

Figure 1. *(a) The solid fraction of A356 alloy that varies with temperature and (b) the viscosity curve of A356 alloy that varies with temperature.*
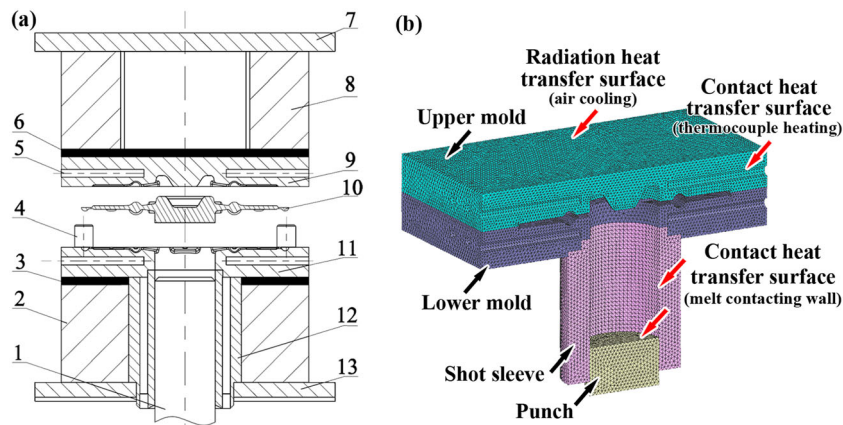

Figure 2. *(a) The rheological squeeze casting mold assembly diagram and (b) the finite element model.*

Table 2. Components in Figure 2a

No.	1	2	3	4	5	6	7
Name	Punch	Lower mold frame	Thermal insulation cotton	Guide pin	Heating channel	Thermal insulation cotton	Moving clamp plate

No.	8		9	10	11	12	13
Name	Upper mold frame		Upper mold	Casting	Lower mold	Vertical shot sleeve	Bottom clamp plate

fraction of A356 alloy at various temperatures was calculated using the Thermo-Calc 2024 software, as illustrated in Figure 1a. And Figure 1b depicts the viscosity curve of A356 alloy varies with temperature. The curves presented in Figure 1 serve as the initial input for the ProCAST software.

Figure 2 and Table 2 present the assembly diagram and the corresponding finite element model of the mold employed in the rheological squeeze casting process. Additionally, the material of mold is H13 hot work die steel. Figure 2b shows the simplified finite element model, for the auxiliary components that only serve for support and positioning, and do not directly affect the numerical simulation results. Thermal

properties include features such as density, specific heat, enthalpy, latent heat, heat transfer coefficient, and viscosity. These features are primarily based on a simple dual-phase model to calculate such characteristics:[33]

$$P = \sum_i x_i P_i + \sum_i \sum_{j>i} x_i x_j \sum_v \Omega_{ij}^v (x_i - x_j)^v \qquad \text{Eqn. 1}$$

Where P represents the thermophysical properties of the phase, P_i represents the thermophysical properties of the pure elements in the phase, x_i and x_j represent the molar fractions of the elements in the phase, v is a variable for the binary interaction parameter ($0 \leq v \leq 2$), an Ω_{ij}^v represents

the binary interaction parameter (mol·L^{-1}). The three-dimensional transient flow and heat transfer of the metal melt are considered, and a set of control equations based on mass, momentum, and energy balance are established. In addition, the influence of gravity must be taken into account, so a gravity term is added to the momentum equation. This allows the equation to be applicable to both the mushy region and the solid-phase region. The control equations are as follows:[34]

    1)   Mass conservation equation:

$$\frac{\partial \rho}{\partial t} + \frac{\partial(\rho u)}{\partial x} + \frac{\partial(\rho v)}{\partial y} + \frac{\partial(\rho w)}{\partial z} = 0 \qquad \text{Eqn. 2}$$

    2)   Momentum conservation equation:

$$\frac{\rho}{f_l}\frac{\partial u}{\partial t} + \frac{\rho}{f_l^2}u\frac{\partial u}{\partial x} + v\frac{\partial u}{\partial y} + w\frac{\partial u}{\partial z} = -\frac{\partial P}{\partial x} + \rho g_x + \frac{\partial}{\partial x}\left(\frac{u}{f_l}\frac{\partial u}{\partial x}\right)$$
$$+ \frac{\partial}{\partial y}\left(\frac{u}{f_l}\frac{\partial u}{\partial y}\right) + \frac{\partial}{\partial z}\left(\frac{u}{f_l}\frac{\partial u}{\partial z}\right) - \left(\frac{u}{K}\right)U$$

$$\text{Eqn. 3}$$

    3)   Energy conservation equation:

$$\rho\frac{\partial H}{\partial t} + \rho\frac{\partial H}{\partial t}\left(u\frac{\partial T}{\partial x} + v\frac{\partial T}{\partial y} + w\frac{\partial T}{\partial z}\right)$$
$$= \frac{\partial}{\partial x}k_T\frac{\partial T}{\partial x} + \frac{\partial}{\partial y}k_T\frac{\partial T}{\partial y} + \frac{\partial}{\partial z}k_T\frac{\partial T}{\partial z} \qquad \text{Eqn. 4}$$

$$HT = \int_0^T C_p(T)dT + L(1 - f_s) \qquad \text{Eqn. 5}$$

In the equation, u, v, and w are the velocity components in the x, y, and z directions, respectively (m/s), t is time (s), f_l and f_s are the liquid and solid fractions, P is pressure (Pa), g_x is the gravitational component in the z direction (m/s^2), ρ is density (kg/m^3), U is absolute viscosity (Pa·s), k_T is the heat transfer coefficient (W·m^{-2}·K^{-1}), C_p is specific heat (J/(kg·K)), L is the latent heat of solidification (J/kg), T is the nodal temperature (K), and H is the enthalpy (J/mol).

To ensure that the numerical simulation results of the rheological squeeze casting stage can most accurately reflect the experimental results,[35] the following initial and boundary conditions were established based on previous research results and the comparative analysis of experimental and the numerical simulation results:

    1)   As illustrated in Figures 2b and 3c, the semi-solid slurry was slowly poured into the vertical shot sleeve following homogenization treatment, resulting in heat transfer between the semi-solid slurry and the walls of the vertical shot sleeve and the punch. The heat transfer coefficient was set to 1000 W·m^{-2}·K^{-1}.

    2)   The contact heat transfer occurring at the contact between the A356 alloy semi-solid slurry and the mold cavity was assigned a heat transfer coefficient of 1000 W·m^{-2}·K^{-1}.

    3)   Temperature function related to time was applied at the heating channel positions corresponding to the upper and lower mold to control the mold temperature.

The Forming Process of Rheological Squeeze Casting

Figure 3 illustrates a schematic diagram of the preparation of A356 alloy semi-solid slurry, along with the forming process of rheological squeeze casting. Table 3 presents the parameter settings for the forming process. The process of A356 alloy semi-solid rheological squeeze castings mainly includes the following four steps:

    1)   Melting and purification process. 2.5 kg ± 100 g of A356 alloy was weighed and heated to 715 °C ± 2 °C in an intermediate frequency induction furnace. Subsequently, 12.5 g ± 0.5 g of C_2Cl_6 powder was added to the melt for degassing to obtain a pure melt. Finally, the melt was air-cooled to 670 °C ± 1 °C.

    2)   The A356 semi-solid slurry preparation process. The instantaneous undercooling-induced nucleation of the semi-solid slurry preparation equipment was set at a tilt angle of 45°, and the real-time flow rates of the upper and lower water tanks were adjusted to 30 mL/s and 35 mL/s, respectively. Experimental research indicates that the use of this equipment allows the A356 melt to achieve a significant temperature drop (≥ 60 °C) in a very short period, thereby achieving an exceptionally high cooling rate (as shown in Figure 3a). The A356 alloy semi-solid slurry with a solid-phase fraction of approximately 0.19 was collected using a preheated graphite crucible maintained at a temperature of 500 °C, as illustrated in Figure 3b.

    3)   Homogenization treatment process. After collecting the A356 semi-solid slurry in the preheated crucible at 500 °C, a short stabilization treatment of 15s ± 2s was performed.

    4)   Rheological squeeze casting process. As shown in Figure 3c and Table 3, each experiment utilized a consistent volume of A356 alloy semi-solid slurry, which was slowly poured into the vertical shot sleeve of the bottom injection squeeze casting machine. Subsequently, after completing the mold-closing operation, the punch moved upward to push the semi-solid slurry in the vertical shot sleeve to fill the mold cavity at a preset speed (filling speed) while maintaining the mold temperature at a preset value. After holding the pressure for 10 ± 1s and maintaining it in mold for 2.5 ± 5 min, the casting was removed and water-cooled to room temperature.
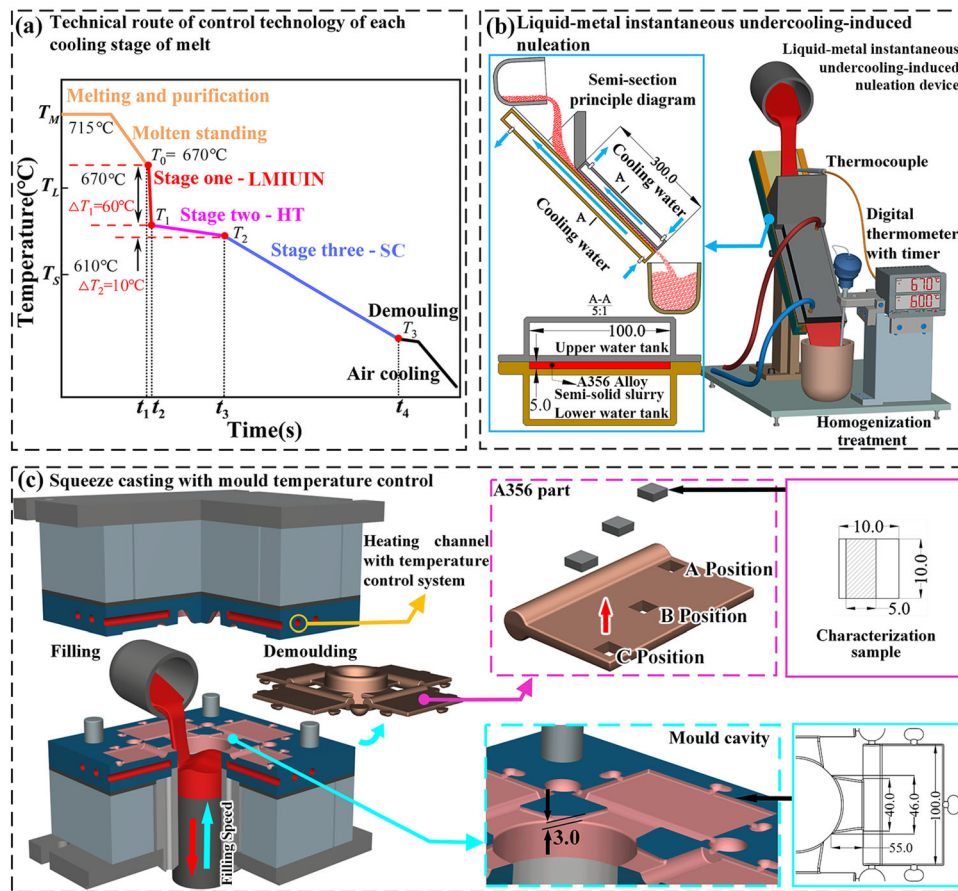
Figure 3. Schematic diagram of semi-solid slurry preparation and rheological squeeze casting process for A356 alloy.

Table 3. Experimental Process Parameters for A356 Alloy Rheological Squeeze Casting Process

No.	Forming specific pressure (MPa)	Mold temperature (°C)	Filling speed (mm/s)
1	125	200	10
2	125	200	15
3	125	200	20
4	125	250	10
5	125	250	15
6	125	250	20
7	125	300	10
8	125	300	15
9	125	300	20
10	125	350	15
11	125	350	20
12	125	350	25

Microstructure Analysis Method

To investigate the impact of different process parameters on the microstructure of A356 alloy rheological squeeze castings, samples were machined for microstructure observation as depicted in Figure 3c. The microstructure observation samples were polished with 280#, 400#, 600#, 800#, and 1000# metallographic sandpapers successively, and then mechanically polished with 500 nm diamond polishing liquid. Subsequently, Kellers etchant solution (95 mL H_2O+2.5 mL HNO_3+1.5 mL HCl+1 mL HF) was used to etch for 10–12 s, followed by immediate rinsing with anhydrous ethanol and blow-drying.

For the microstructure and elemental distribution observation of the castings, a Nikon ECLIPSE MA200 metallurgical optical microscope (OM) was used to observe the grain morphology of the samples. The microstructure was characterized, and the various components were quantitatively analyzed utilizing a Chinainstru & Quantumtech (Hefei) SEM 5000 Pro field emission scanning electron microscope (FESEM) and its attached Oxford Instruments Xplore30 energy-dispersive spectrometer (EDS). The phase structure of the A356 alloy casting was characterized using a Rigaku MiniFlex 600 X-ray diffractometer (XRD). To establish the size (μm) and volume fraction (%) of the various phases in the samples, 10–15 random fields were captured in the environment of the metallurgical microscope (Nikon ECLIPSE MA200) and then colored using
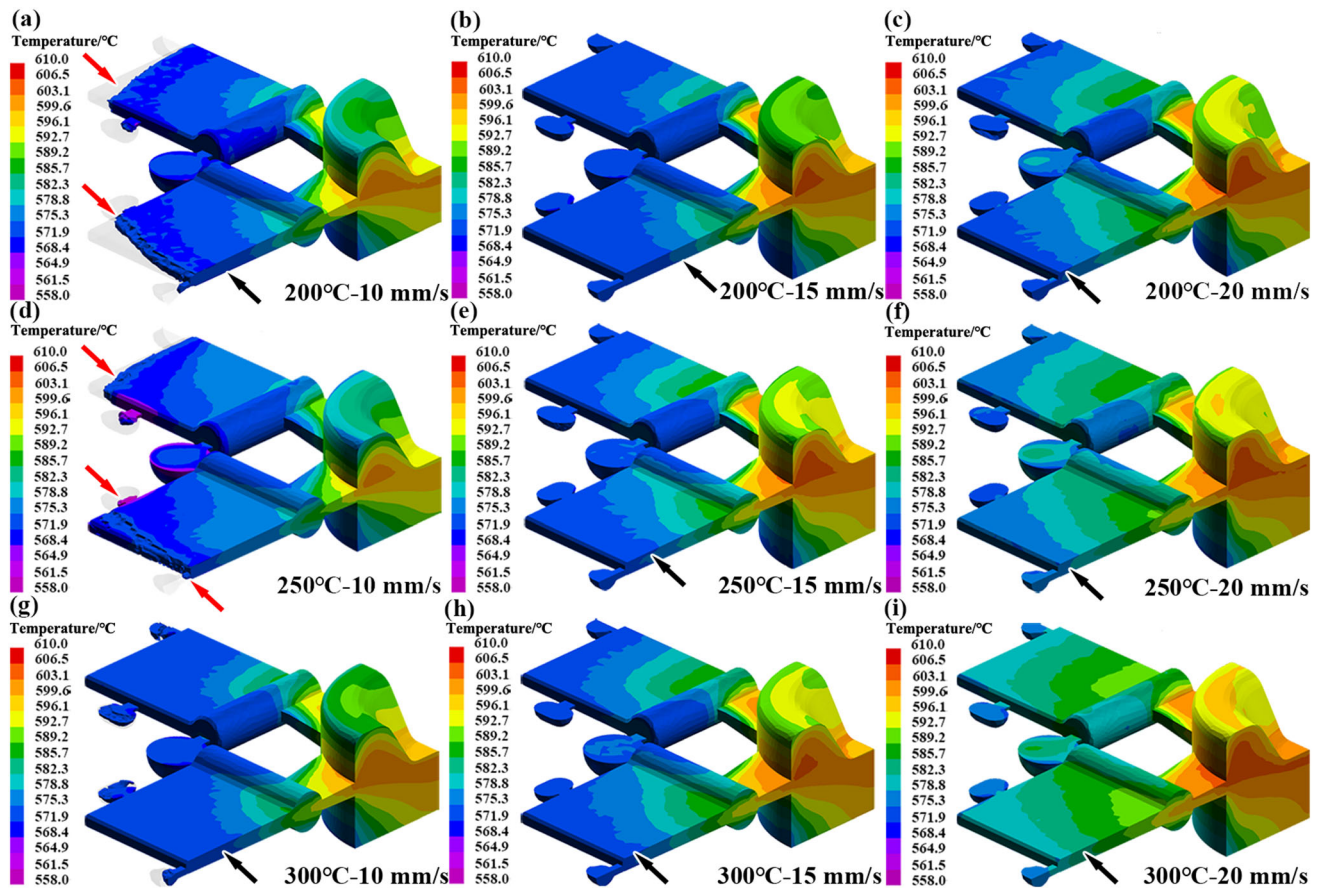
Figure 4. Temperature field distribution of A356 alloy rheological squeeze castings with different combinations of process parameters.

Adobe Photoshop 2022 software. Subsequently, statistical analysis was carried out using Image-Pro Plus 6.0 software. The formula is as follows:[36]

$$d_m = \frac{2}{n}\left(\sqrt{\frac{S_1}{\pi}} + \sqrt{\frac{S_2}{\pi}} + \cdots + \sqrt{\frac{S_n}{\pi}}\right) \qquad \text{Eqn. 6}$$

where d_m is the average diameter and S_1, S_2, …, S_n are the areas of the 1st, 2nd, ..., nth grains, respectively.

Result and Discussion

Temperature Field Distribution Law of A356 Alloy Rheological Squeeze Castings

As shown in Figures 4 and 5, to clarify the temperature field distribution and the solid-phase fraction distribution of the casting surface and cross section under different process parameter conditions, a quarter of the casting was sectioned for comparative analysis after filling.

Figures 4a, d, g and 5a, d, g illustrate that at a filling speed of 10 mm/s and a relatively low mold temperature (200–250 °C), extensive incomplete filling defects occurred in areas far from the sprue and overflow groove (indicated by the red arrows). Moreover, the distribution of the solid-phase fraction in the casting was extremely uneven, with the solid-phase fraction far from the sprue approached nearly 100% (indicating complete solidification), while the solid-phase fraction near the sprue direction was concentrated in the range of 37–56%. This indicates that under the combination of excessively low filling speed and low mold temperature, it was no longer possible to provide a continuous and stable filling capacity. As demonstrated in Figures 4a–c and 5a–c, with the mold temperature maintained at 200 °C, the casting no longer exhibited obvious incomplete defects as the filling speed increased from 10 to 20 mm/s. The temperature gradient of the casting surface and cross section gradually decreased, and the temperature field distribution gradually tended to be uniform, with the isotherms gradually becoming flatter (indicated by the black arrows). With the filling speed controlled at 15 and 20 mm/s (as shown in Figure 4 b, h, e, f, and i), under higher mold temperature conditions, an increase in filling speed led to a gradual decrease in the temperature gradient of the casting surface and cross section, and a more uniform distribution of the temperature field and solid-phase fraction.
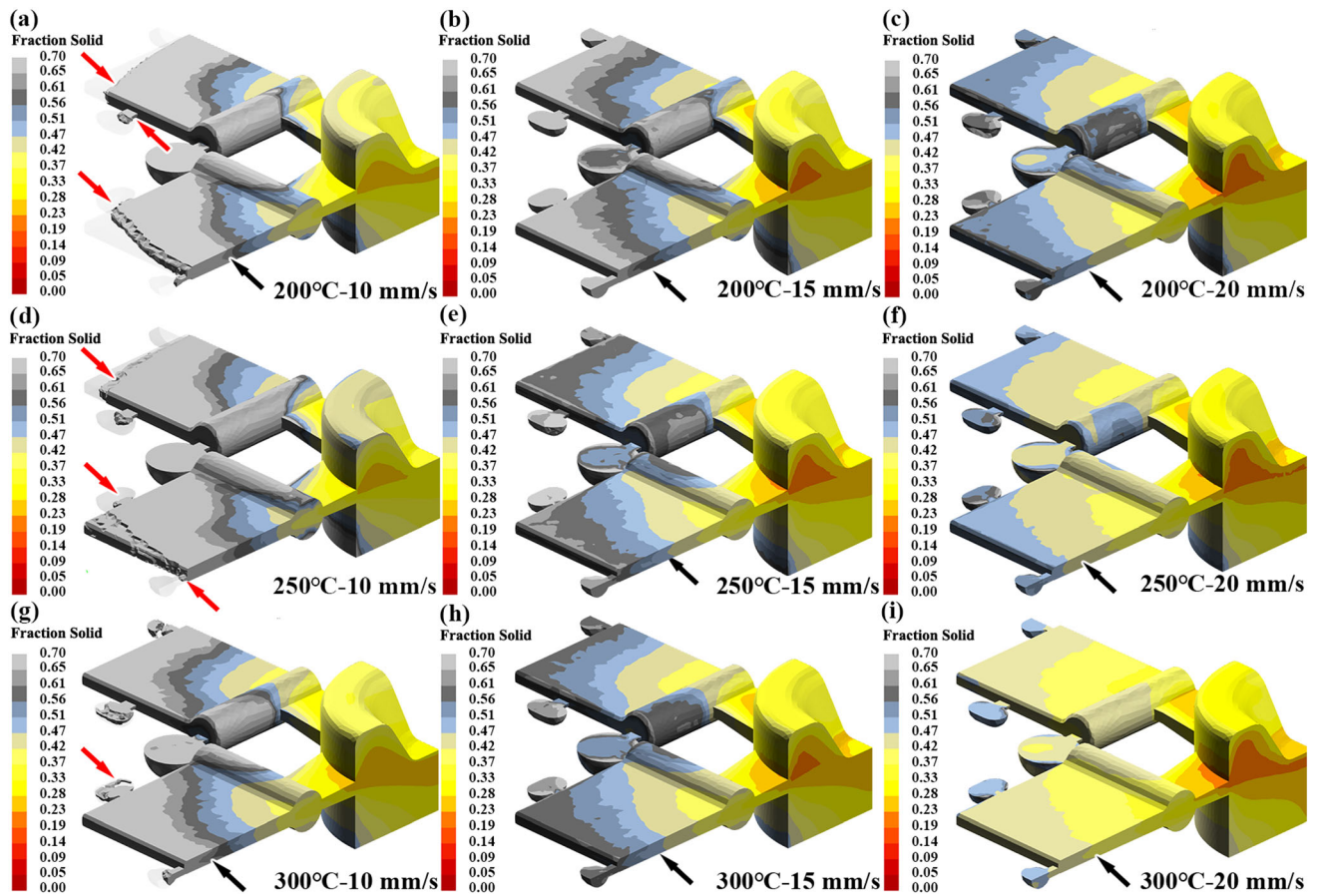
Figure 5. Solid-phase fraction of A356 alloy rheological squeeze castings with different combinations of process parameters.

Table 4. Design of Orthogonal Table L9(3)³

No.	Forming process parameters		Numerical simulation results	
	Mold temperature (°C)	Filling speed (mm/s)	Maximum temperature difference within the castings (°C)	High solid-fraction volume share (%)
1	200	10	29.30	70.20
2	200	15	24.33	42.10
3	200	20	19.13	4.62
4	250	10	22.20	59.40
5	250	15	18.60	13.16
6	250	20	10.40	2.12
7	300	10	20.80	49.22
8	300	15	8.10	6.20
9	300	20	17.20	1.17

sprue to the far end. Although increasing the mold temperature reduces the temperature gradient and promotes uniformity within temperature field, the average maximum temperature difference of the casting from the near sprue position to the farthest position still reaches approximately 30 °C (as shown in Figure 4a–c). Moreover, with a filling speed of 20 mm/s and a mold temperature of 250 °C, the overall temperature field distribution of the casting significantly improves compared to the conditions with lower filling speed and lower mold temperature, with the maximum gradient only being 20.5 °C. Notably, when the mold temperature is raised to 300 °C and coupled with a higher filling speed (20 mm/s), the temperature gradient of the casting is the smallest among the nine orthogonal experiments, at just 13.9 °C, and the temperature field distribution is the most uniform.

Based on Table 3, a three-factor, three-level ((L₉(3)³) orthogonal experimental design was established as shown in Table 4, for quantitative analysis described above. The maximum temperature difference within the casting (°C) and volume share (%) of high solid-phase fraction (Fs = 60–100%) molten metal in the casting s were selected as the main evaluation indicators, with three levels for each factor. Furthermore, the impact of individual factors on the

Similarly, when the same mold temperature is maintained and the effects of different filling speeds on the temperature field of the castings are compared, it is observed that under lower filling speed conditions, the temperature field distribution of the casting is highly uneven from near the

Table 5. Results of Range Analysis

	Maximum temperature difference (°C)		Volume share of high solid-phase fraction (%)	
	Mold temperature (°C)	Filling speed (mm/s)	Mold temperature (°C)	Filling speed (mm/s)
K1	72.76	72.30	116.93	178.83
K2	51.20	51.03	74.68	61.46
K3	46.10	46.73	56.59	7.91
k1	24.26	24.10	38.98	59.61
k2	17.07	17.01	24.89	20.49
k3	15.37	15.58	18.86	2.64
R	8.89	8.52	20.11	56.97

Figure 6. The effect of individual factors on the characteristics of A356 alloy rheological squeeze castings.

maximum temperature difference within the casting (°C) and the volume share of high solid-phase fraction (Fs = 60–100%) molten metal in the casting was assessed through individual factor analysis. In Table 5, K_i ($i = 1, 2, 3$) represents the sum of the level values of each factor in Table 4, k_i ($i = 1, 2, 3$) represents the average value of the level values, and the range value (R) is the difference between the maximum and minimum values of the average values for each level. Range analysis was employed to identify the most influential factors affecting the evaluation indicators. Additionally, a graphical representation (Figure 6) was used to visually illustrate the effects of individual factor on the maximum temperature difference within the casting (°C) and the volume share of high solid-phase fraction (Fs = 60–100%) molten metal in the casting, providing an intuitive reflection of the results from Table 4.

Figure 6 illustrates a distinct decreasing trend in both the maximum temperature difference within the casting (°C) and the volume share of high solid-phase fraction (Fs = 60–100%) molten metal as the mold temperature increases from 200 to 300 °C and the filling speed increases from 10 to 20 mm/s. Notably, when the filling speed is raised from 10 to 15 mm/s, the volume share of high solid-phase fraction (Fs = 60–100%) molten metal decreases from 59.61 to 20.49%. Furthermore, with a further increase in the filling speed to 20 mm/s, the volume share of high solid-phase fraction (Fs = 60–100%) molten metal exhibits a sharp decline, dropping to 2.64%. The filling speed has a significantly greater influence on both evaluation indicators compared to the mold temperature.

By analyzing Figure 6 in conjunction with Table 5, the following conclusions can be drawn:

(a) At filling speeds of 10–15 mm/s and mold temperatures of 200–250 °C, a discernible temperature gradient and a relatively high-temperature field distribution are evident along the cross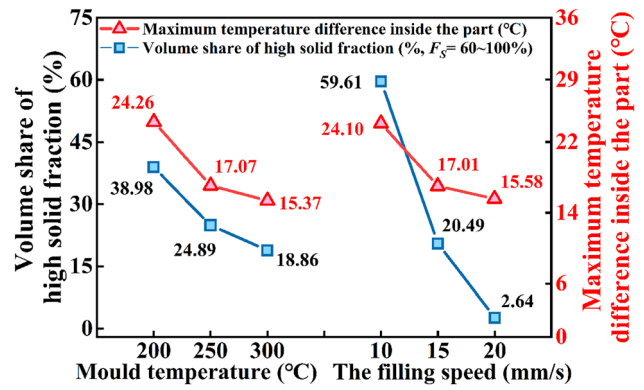 section and surface of the castings. (b) With an increase in filling speed and mold temperature, the uniformity of the temperature distribution within the casting significantly improves. (c) The effect of mold temperatures and filling speeds on the maximum temperature difference within the casting demonstrates similar significance, whereas the effect of filling speed on the volume share of high solid-phase fraction (Fs = 60–100%) molten metal is markedly more significant, exceeding that of mold temperature. (d) The order of significance for the maximum temperature difference within the casting is: mold temperature > filling speed, while the order of significance for volume share of high solid-phase fraction (Fs = 60–100%) molten metal (%) is: filling speed > mold temperature.

Based on the above analysis, it can be inferred that at a forming specific pressure of 125 MPa, the optimal process parameters for filling speed (10–20 mm/s) and mold temperature (200–300 °C) are 25 mm/s and 300 °C, respectively.

The Influence of the Forming Process on the Temperature Field, Velocity Field, and Solid-Phase Fraction of the Casting

The preceding analysis indicates that process parameters significantly affect the temperature distribution, microstructure, and solute homogenization during the casting filling process.[24] Combining these findings with the trend illustrated in Figure 6 suggests that the optimal process parameter set is situated on the boundary of the suggested range in the orthogonal experimental design. It is reasonable to surmise that a further increase in mold temperature and filling speed are likely to enhance the synergy between solid and liquid phases, as well as improve the uniformity of temperature and velocity fields, and the distribution of solid-phase fractions in the A356 castings. The previous analysis indicated that the impact of filling speed outweighs that of mold temperature. Therefore, considering the casting filling process at a mold temperature of 250 °C and a filling speed of 10 mm/s as the reference group (referred to as A356-250-10), three additional

sets of samples—A356-350-15, A356-350-20, and A356-350-25—are introduced, and the numerical simulation results of these four sets of samples are compared and analyzed.

As depicted in Figure 7, the temperature field, solid-phase fraction, and velocity field distribution of A356-250-10 sample at different instants during the filling process are shown. After A356 alloy semi-solid slurry was poured into the shot sleeve, the punch began to move upward at the initial time ($t = 0$ s). At $t = 2.9$ s, the semi-solid slurry entered the mold cavity, exhibiting a distinct "layered" flow characteristic, progressing layer by layer into the interior of the mold cavity, as depicted in Figure 7a. Illustrated in Figure 7a-2, the transient velocity of the molten metal is low at this moment. Additionally, in the initial stage of the filling, the solid-phase fraction of the molten metal is relatively low ($\sim 23.0\%$). Figure 7b, c reveals that under the action of the punch, the molten metal

steadily moves within the mold cavity away from the gate direction.

During this process, the molten metal experiences a significant decrease in temperature at the front end during the filling process. As shown in Figure 7b-2, c-2, under this process condition, the instantaneous velocity at the front of the molten metal is about 0 mm/s, signifying that the excessively low filling speed in this scenario prevents continuous filling of the molten metal. The significant decrease in temperature at the front end of the molten metal leads to a decrease in fluidity due to the increase in viscosity and solid-phase fraction (as indicated by the black arrow 2). The decrease in fluidity and increase in viscosity in turn restrict the velocity of the molten metal (as indicated by the black arrow 1 and arrow 3). Additionally, the longer the molten metal remains in the mold cavity, the stronger the heat exchange between the molten metal and the mold cavity, resulting in a larger temperature drop, higher viscosity, poorer fluidity, and higher solid-phase fraction.
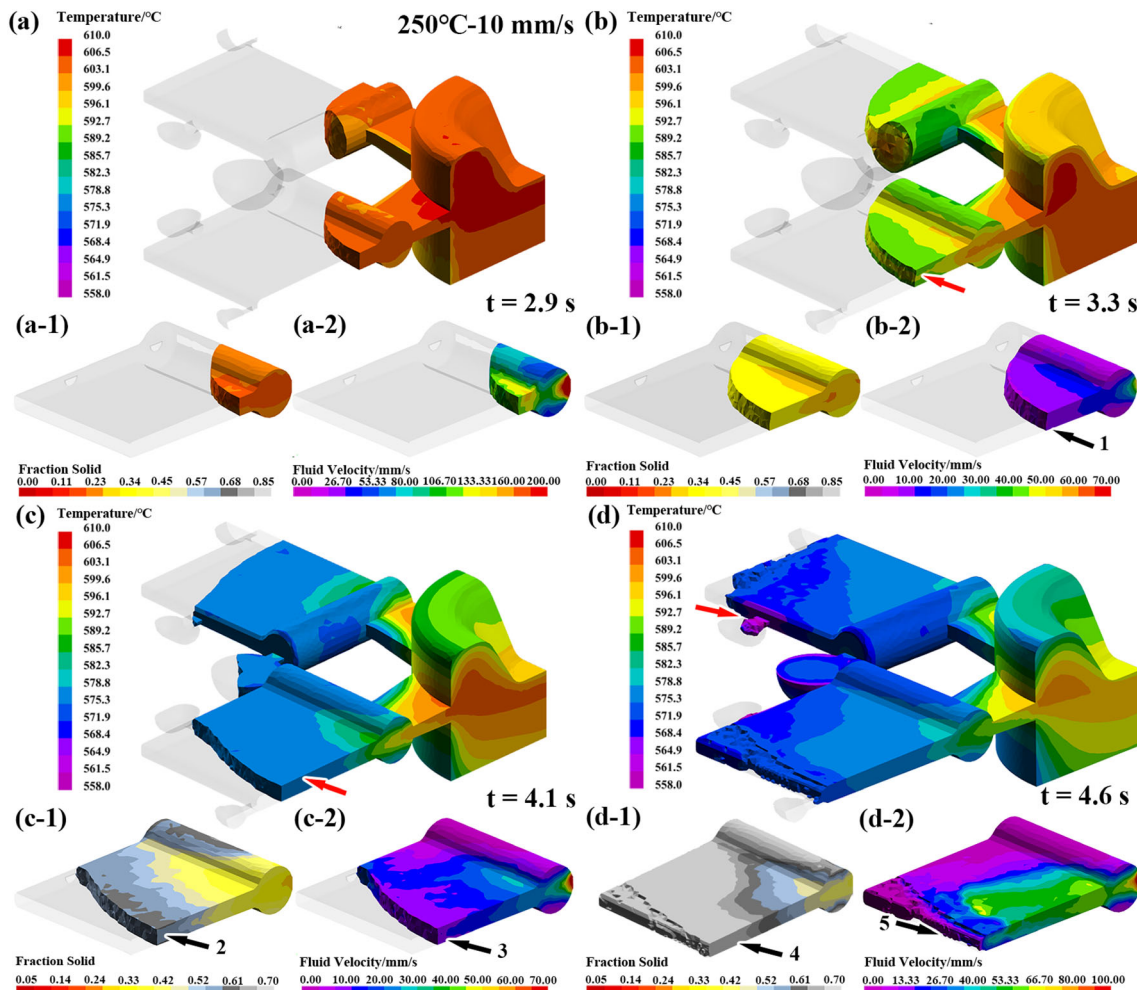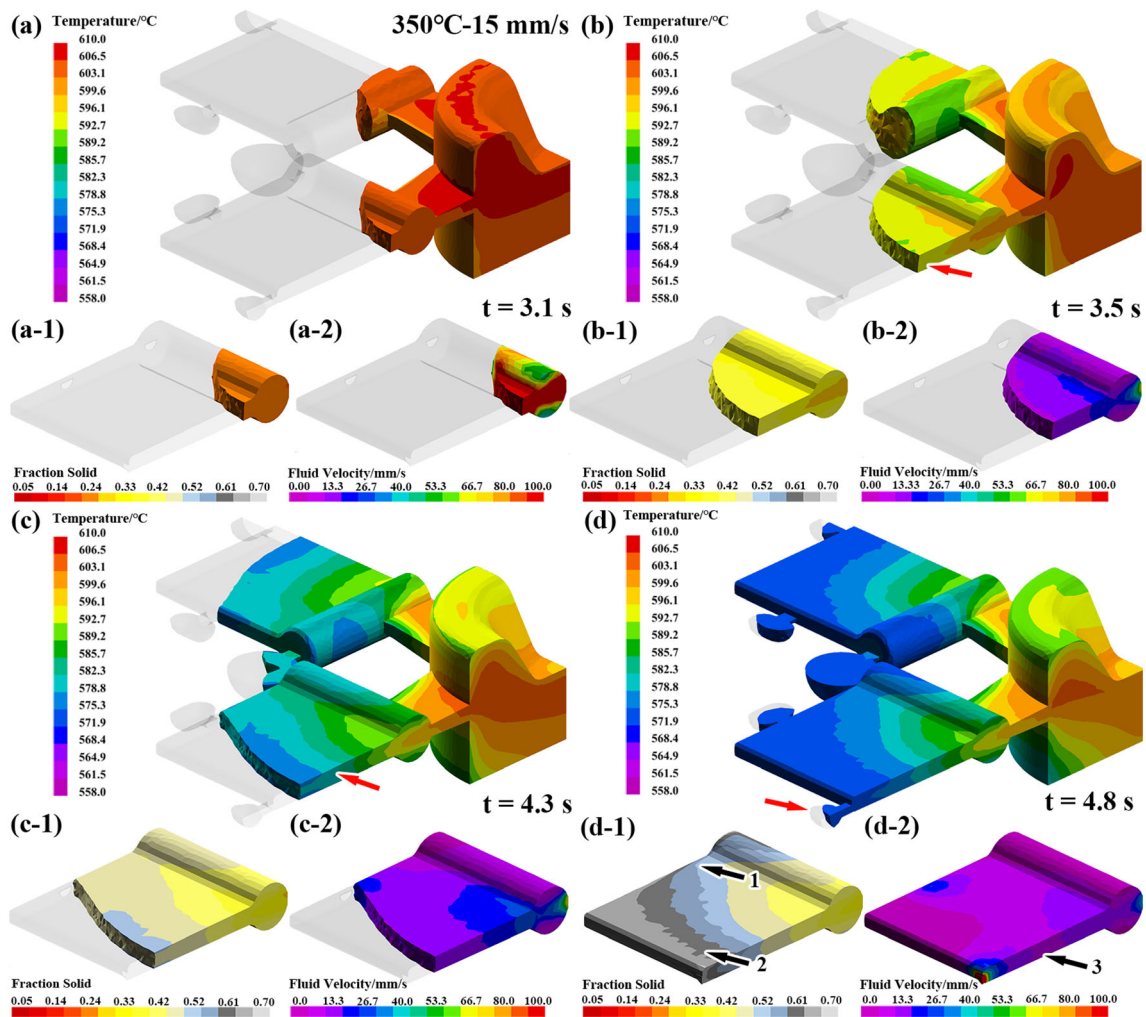

Figure 7. Distribution of temperature, solid-phase fraction, and velocity fields of A356 alloy at different moments during the rheological squeeze casting process at a mold temperature of 250 °C and a filling speed of 10 mm/s: (a) t = 2.9 s, (b) t = 3.3 s, (c) t = 4.1 s, (d) t = 4.6 s.

Figure 8. Distribution of temperature, solid-phase fraction, and velocity fields of A356 alloy at different moments during the rheological squeeze casting process at a mold temperature of 350 °C and a filling speed of 15 mm/s: (a) t = 3.1 s, (b) t = 3.5 s, (c) t = 4.3 s, (d) t = 4.8 s.

Figure 7d illustrates the instantaneous temperature field, velocity field, and solid-phase fraction distribution map before the completion of the filling process. Since the mold temperature and filling speed are both low, approximately 80% of the molten metal has a solid-phase fraction higher than 61%, while the remaining molten metal has a solid-phase fraction concentrated between 33 and 42%. At this stage, the instantaneous velocity at the front end of the molten metal is almost 0 mm/s, whereas the instantaneous velocity of the rear part of the molten metal stays between 40 and 55 mm/s (as shown in Figure 7d-2). This implies that, before the end of the filling, the rear molten metal with a low solid-phase fraction pushes the front molten metal with a high solid-phase fraction forward, resulting in a poor overall solid–liquid flow synergy. Hence, the combination of low mold temperature and low filling speed will considerably compromise the microstructure uniformity of the casting.

Based on Figure 7a-1, a-2, b-1, b-2, and Figure 8a-1, a-2, b-1, b-2, after increasing the mold temperature to 350 °C,

during the early stage of filling, there was no significant change in the flow characteristics and temperature gradient of the molten metal. However, by comparing Figure 7c with Figure 8c, it is evident that with a slight increase in the mold temperature and filling speed, it effectively ensured that the molten metal could maintain a higher temperature when reaching the same position, and significantly reduced the temperature gradient inside the castings.

Moreover, comparing Figure 7c-1 with Figure 8c-1 indicated a significant decrease in the solid-phase fraction of the semi-solid slurry at the same position in the mold cavity, along with a more uniform distribution. Also, it was noted that in comparison with the A356-250-10 sample, aside from a few regions where the solid-phase fraction reached 65%, in other areas the solid-phase fraction remained basically remained within the range of 33% and 52%. Further comparison and analysis of Figure 7d-1, d-2 with Figure 8d-1, d-2 reveal that a slight increase in mold temperature and filling speed led to a significant
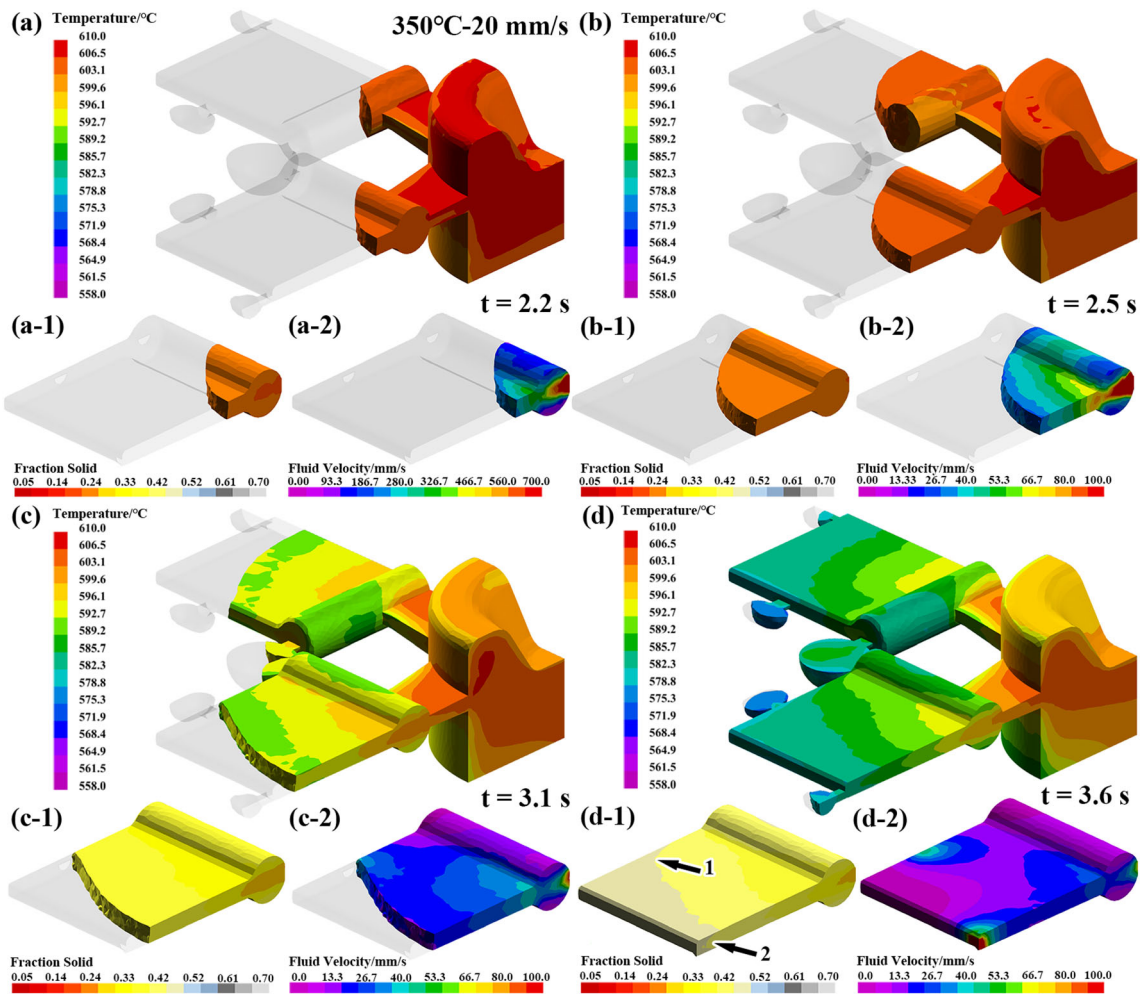
Figure 9. *Distribution of temperature, solid-phase fraction, and velocity fields of A356 alloy at different moments during the rheological squeeze casting process at a mold temperature of 350 °C and a filling speed of 20 mm/s: (a)* t = 2.2 s, *(b)* t = 2.5 s, *(c)* t = 3.1 s, *(d)* t = 3.6 s.

homogenization of the temperature field distribution. This indicates that the distribution of the solid-phase fraction in the casting, both along the filling speed direction and the section direction, became noticeably more uniform, mostly concentrated in the range of 33–42%.

Lastly, a comparison between the region indicated by the black arrow 5 in Figure 7d-2 and the region indicated by arrow 3 in Figure 8d-2 showed that a higher filling speed facilitated a more uniform and rapid filling of the entire mold cavity. Consequently, under the condition of a mold temperature of 350 °C, there were nearly no instances of an instantaneous velocity of 0 mm/s, with the front end of the molten metal maintaining a speed of about 13.3 mm/s.

In the investigation of the influence of the filling speed on the semi-solid slurry A356 filling process, the mold temperature was maintained at 350 °C, and the evolution patterns of the temperature field, instantaneous velocity field, and solid-phase fraction of the semi-solid slurry during the filling process were analyzed at filling speeds of

15, 20, and 25 mm/s. A notable decrease in the temperature gradient at the front end of the molten metal was observed as the filling speed increased, as indicated in Figures 8a–c, 9a–c, and 10a–c. Additionally, the uniformity of the distribution of the solid-phase fraction of the molten metal displayed a clear improvement trend, as evident in Figures 8c-1, c-2, 9c-1, c-2, and 10c-1, c-2. At a mold temperature of 350 °C and a filling speed of 15 mm/s, 90% of the molten metal's solid-phase fraction was in the range of 33–47%, with only about 5% of the molten metal in the high solid-phase fraction range ($\sim$ 61%). When the filling speed increased to 20 mm/s and above, the molten metal was almost entirely within the 33% solid-phase fraction range, and the front end of the molten metal almost did not exhibit any regions with an instantaneous velocity of 0 mm/s.

Finally, at the end of the filling process (as shown in Figures 7d, d-1, d-2, 8d, d-1, d-2, 9d, d-1, d-2, 10d, d-1, d-2), the influence of the filling speed on the molten metal was very significant. At a filling speed of 15 mm/s, as indicated
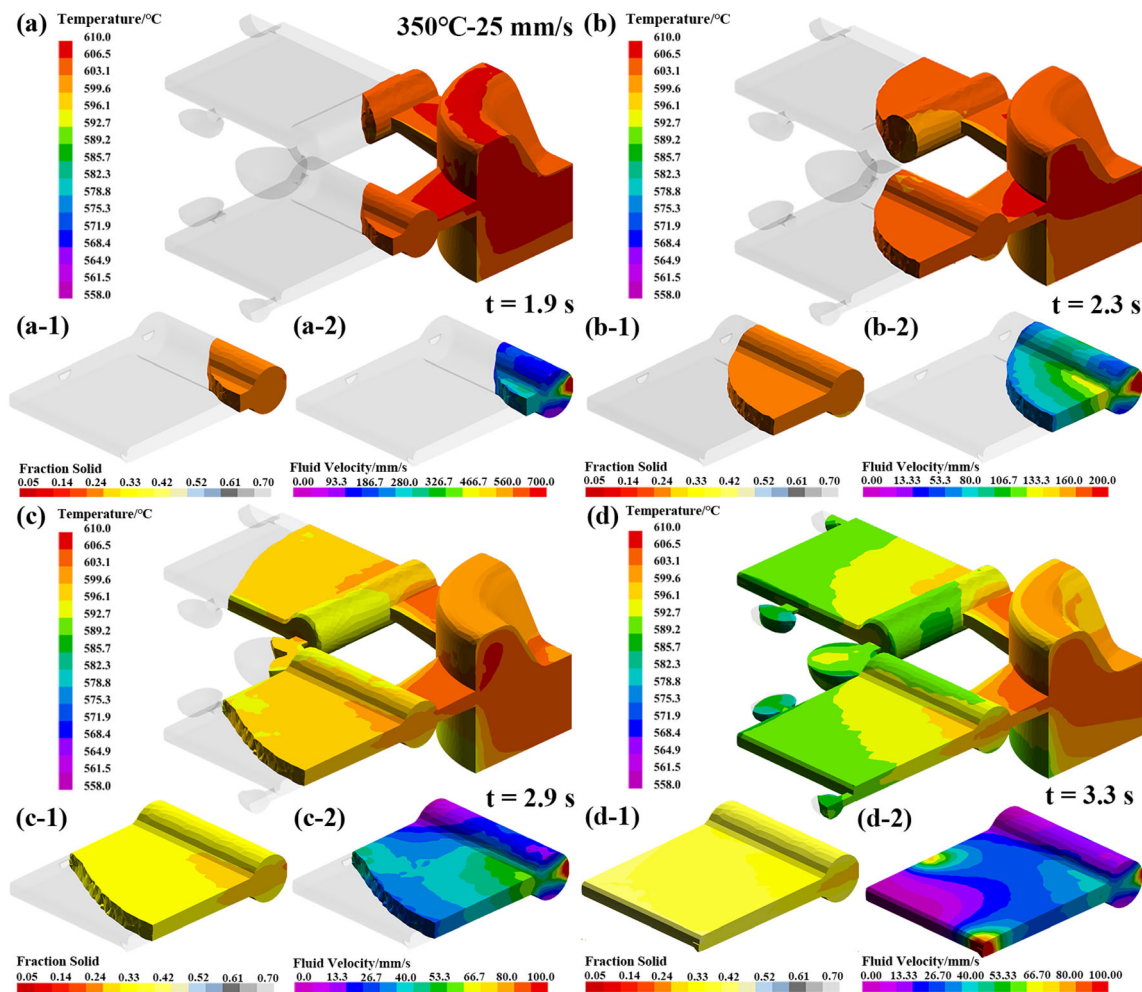
Figure 10. *Distribution of temperature, solid-phase fraction, and velocity fields of A356 alloy at different moments during the rheological squeeze casting process at a mold temperature of 350 °C and a filling speed of 25 mm/s:(a)* t = 1.9 s, *(b)* t = 2.3 s, *(c)* t = 2.9 s, *(d)* t = 3.3 s.

by arrows 2 in Figure 8, the solid-phase fraction of nearly 60% of the volume of the molten metal was above 56%, and the excessively high difference in solid-phase fraction could likely lead to a decrease in the solid/liquid flow coordination, making it easy for macroscopic quality defects such as cold shuts to form in regions along the solid-phase fraction lines indicated by arrow 1 in Figure 8d-1. This subsequently led to significant differences in the microstructure of different regions of the casting. However, by increasing the filling speed to 20 mm/s, apart from a small area on the surface of the molten metal where the solid-phase fraction reached 47%, the solid-phase fraction in other areas remained at around 33%. With a filling speed of 25 mm/s, the distribution of the solid-phase fraction in the casting was very uniform, almost entirely concentrated in the range of 28–33%, both along the filling speed direction and the section direction. Figures 8d-2, 9d-2, and 10d-2 reveal that the escalation in filling speed facilitated a more uniform and rapid filling of the entire mold cavity by the molten metal. Consequently, at a filling speed of 20 mm/s, the area with an instantaneous velocity

of 0 mm/s notably reduced, and at 25 mm/s, there were scarcely any regions with an instantaneous velocity of 0 mm/s.

In summary, the combined effect of a higher mold temperature (350 °C) and increased filling speed (20–25 mm/s) are beneficial for enhancing the stability and uniformity of the internal temperature distribution during the semi-solid slurry filling process, as well as reducing the temperature gradient within the semi-solid slurry.

Microstructure Analysis

Figure 11 depicts the microstructures of A356 alloy rheological squeeze castings components at different locations under the above four process conditions (sampling method as shown in Figure 3c). The microstructure of the casting exhibits significant differences. Specifically, as shown in Figure 12a–c, at filling speeds of 10–15 mm/s, the microstructural morphology at positions A, B, and C of the
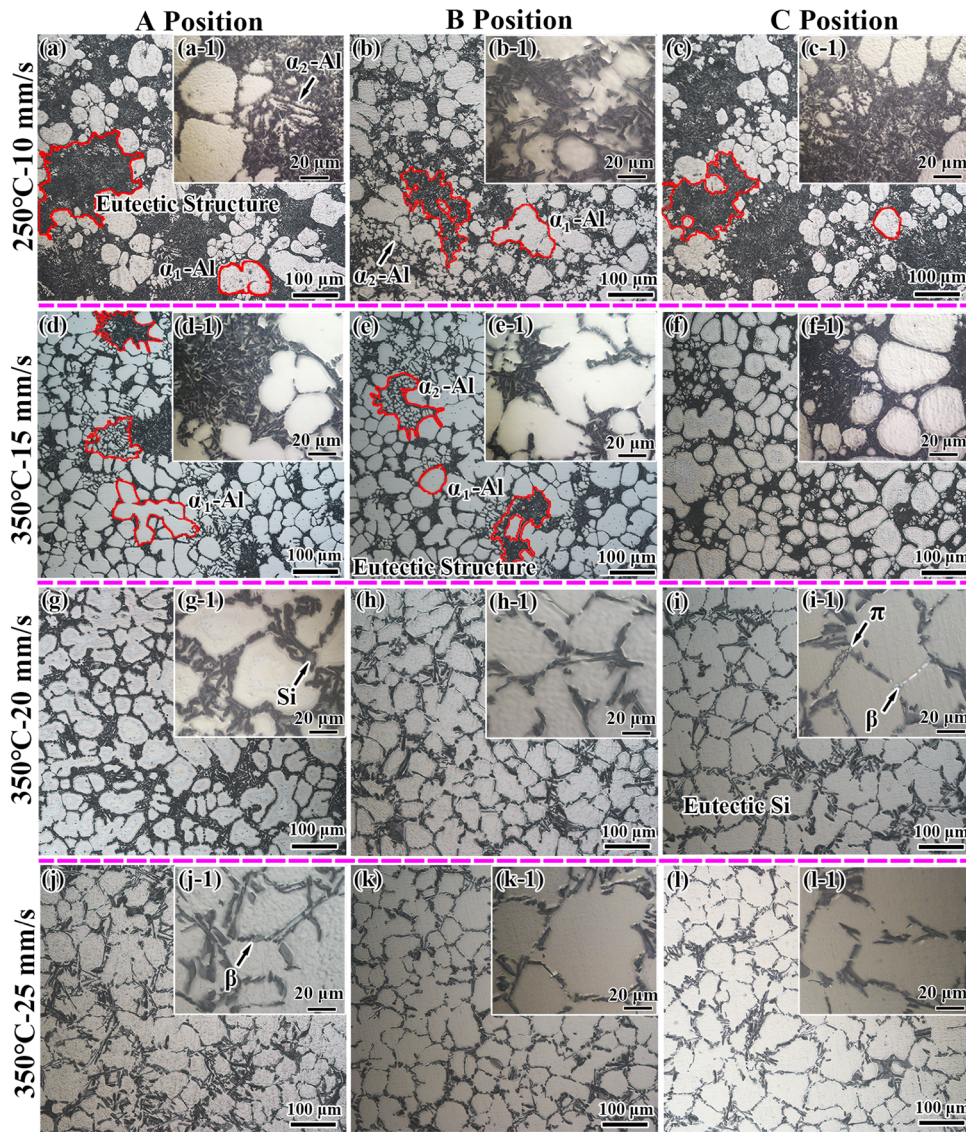
Figure 11. Microstructure of A356 alloy rheological squeeze castings under different process parameters.
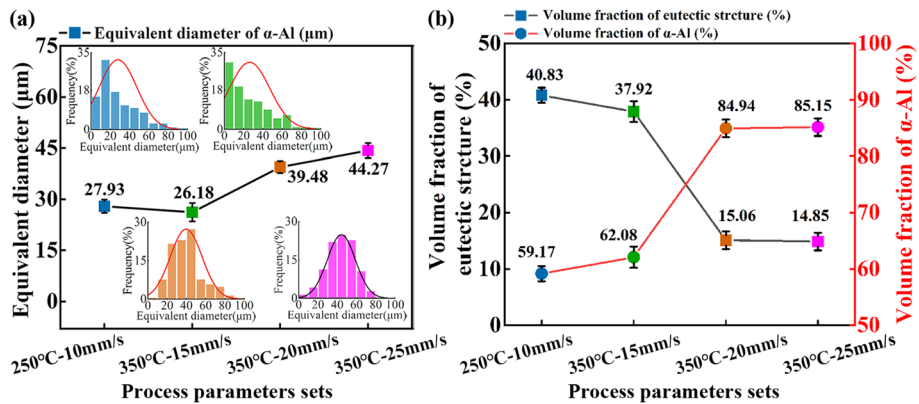

Figure 12. (a) The average equivalent diameter of α-Al phase and (b) the volume fraction of each phase of A356 alloy under different process conditions.
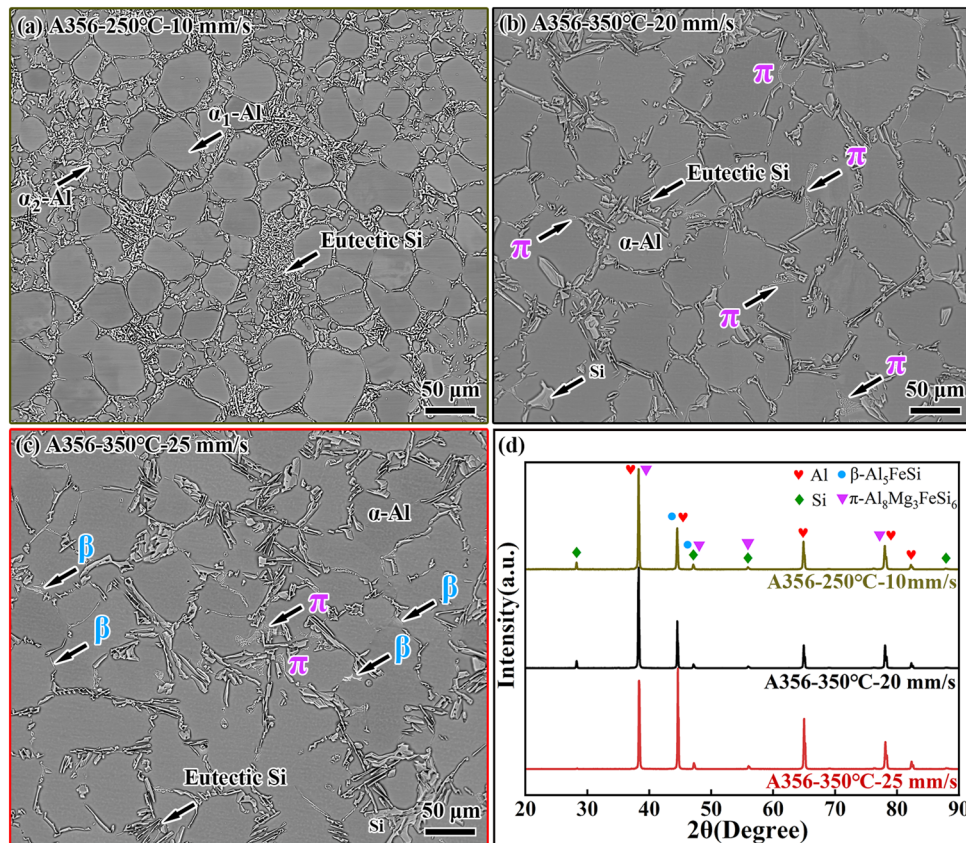
Figure 13. (a)–(c) The FESEM images and (d) XRD pattern of A356 alloy under different process conditions.

samples exhibits typical structures of Al–Si alloy rheological squeeze castings, with near-spherical, ellipsoidal, or small rosette-shaped light gray primary α_1-Al phase grains (referred to as α_1-Al hereinafter).

Additionally, as shown in Figure 11a-1, b-1, and c-1, a small amount of fine dendritic or equiaxed grains can also be observed. These fine grains are secondary α_2-Al grains formed by the residual liquid phase during the solidification process (referred to as α_2-Al phase hereinafter). In addition, there is a high-density interdendritic eutectic structure surrounding the α_1-Al and α_2-Al phases, and the overall microstructure is disorderly, with poor uniformity and circularity of the structure at different locations. As shown in Figure 11d–f, there is a noticeable decrease in the degree of aggregation and content of eutectic structure at three positions in the casting, decreasing from 40.83 to 37.92% (see Figure 13b).

The α_1-Al phase is surrounded by higher content of secondary nucleation, presenting light gray α_2-Al phase grains. This also explains the decrease in the average equivalent diameter of grains in Figure 12a, and from the normal distribution in the figure, it is evident that under low filling speed conditions, the microstructure uniformity of A356 semi-solid rheological squeeze castings is poor, with a low solid-phase fraction (α-Al phase) and a very high content of

eutectic structure. Furthermore, combining Figure 11g–l with Figure 12a reveals that with the increase in filling speed (20–25 mm/s), while the average equivalent diameter of the α-Al phase increases significantly, resulting in a more uniform size, and the α_2-Al grains almost completely disappear. This transformation gradually changes the high-density reticular distribution form of the eutectic Si phase into a dispersed form with a fine rod-like structure.

The microstructure characteristics and phase types of representative samples A356-250-10, A356-350-20, and A356-350-25 under different process conditions were further investigated to provide clarity. Figure 13 illustrates the significant increasing trend in grain size observed in the backscattered electron (BSE) mode of the FESEM (field emission scanning electron microscope) for the mentioned samples. In the A356-250-10 sample, the direct discernment of rich Fe intermetallic compounds is nearly impossible. However, at increased filling speeds among 20–25 mm/s, the ample growth of the α_1-Al phase is clearly observable, along with the presence of the gray script-like π-$Al_8Mg_3FeSi_6$ phase representing Fe-rich intermetallic compounds. Additionally, at 25 mm/s filling speed, the observation of bright needle-like β-Al_5FeSi phase against a background of dark α-Al phase and bright gray Si phase becomes apparent. The XRD analysis of the samples under the three process conditions (see Figure 13d)
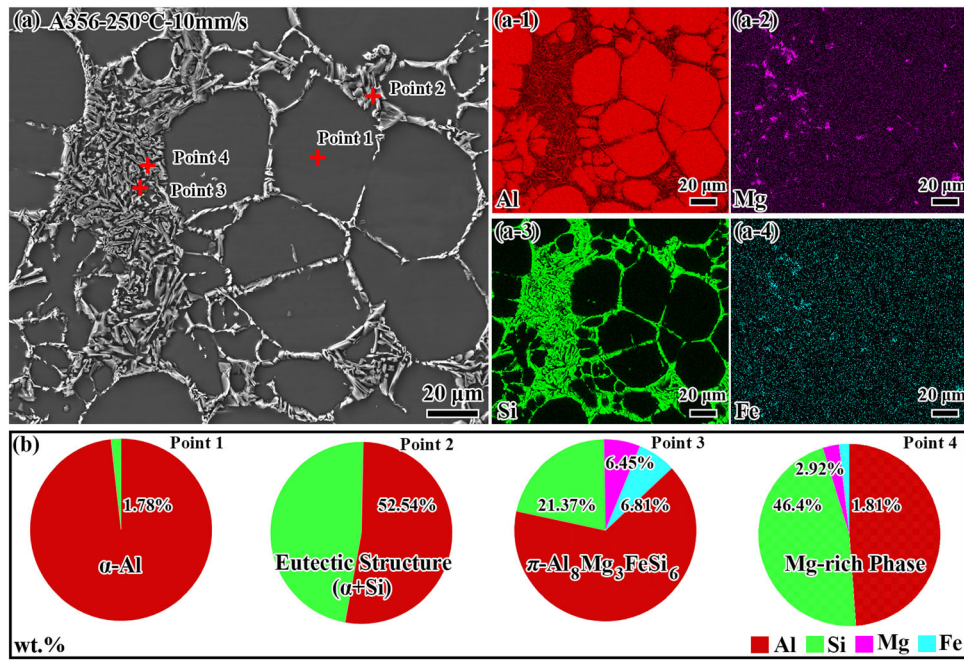
Figure 14. (a) The FESEM image of A356-250-10 sample; (a-1)–(a-4) EDS mapping; (b) EDS results of Figure (a).

reveals a tendency to form the π-$Al_8Mg_3FeSi_6$ phase at filling speeds between 20 and 20 mm/s, while at 25 mm/s, a greater tendency for the high-density β-Al_5FeSi phase to appear is observed. This phenomenon is consistent with Zhao's research conclusions on the relationship between different Fe contents and the microstructure and properties of Al–7Si–0.3Mg.[21]

To support the above viewpoints, microstructural morphology, EDS surface analysis, and EDS point analysis results of A356 alloy rheological squeeze castings under different process conditions are presented in Figure 14, 15, and 16. The EDS surface analysis results clearly illustrate the distribution of Al, Si, Fe, and Mg elements, validating the presence of Mg-rich and Fe-rich intermetallic compounds. Under lower filling speed conditions (10 mm/s), the microstructure is primarily enriched with Mg-rich and Fe-rich intermetallic compounds that coexist with eutectic Si. However, the overall distribution in the matrix is more uniform compared to the other two forming process conditions. While the EDS point analysis results from FESEM in Figure 14a-4 do not directly identify the β-Al_5FeSi phase, it can be inferred from Figure 14b that during the solidification process, the π-$Al_8FeMg_3Si_6$ phase typically grows closely related to the β-Al_5FeSi phase, potentially distributing in a finely dispersed form among the eutectic structure. When the filling speed is increased to 20 mm/s (see Figure 15a-2, a-4, b), the Fe-rich intermetallic compound is mainly in the form of the π-$Al_8Mg_3FeSi_6$ phase, which deforms into a script or labyrinth-like morphology. Upon further increasing the filling speed to 25 mm/s, besides the formation of a large amount of the π-$Al_8Mg_3FeSi_6$ phase near the eutectic Si, it is also possible to observe a high-density Fe-rich β-Al_5FeSi phase in adjacent positions, with a needle-

like or elongated morphology. The morphology characteristics of the Fe-rich intermetallic compounds and the EDS point scan analysis results are basically consistent with the conclusions obtained by Taylor et al.[18,21]

By comparing Figure 14 to Figure 16, it is evident that the degree of aggregation of Mg and Fe elements near the primary α_1-Al phase and eutectic Si gradually increases in the A356-350-20 and A356-350-25 samples compared to the A356-250-10 sample. As depicted in Figure 14a-2, a-4, the aggregation of Mg and Fe elements in the eutectic structure is comparatively lower than in A356-350-20 (see Figure 15a-2, a-4) and A356-350-25 (see Figure 16a-2, a-4), and their dispersion in the α-Al matrix is more uniform. This observation is further supported by the FESEM microstructural images shown in Figure 14a, 15a, and 16a, and the XRD diffraction spectra are presented in Figure 13d, indicating that at a filling speed of 10 mm/s, the diffraction peak corresponding to β-Al_5FeSi is minimal, with the predominant phases being α-Al and π-$Al_8FeMg_3Si_6$. As the filling speed gradually increases, the content of the β-Al_5FeSi phase also increases.

Finally, Figure 16a-2, a-4 reveals a growth trend of the Mg-rich and Fe-rich phases and displays from the eutectic Si phase toward the α-Al phase, leading to the prevalence of the β-Al_5FeSi phase under high filling speed conditions, while the π-$Al_9FeMg_3Si_5$ phase predominates under lower filling speed conditions. Hence, it is inferred that non-equilibrium solidification substantially modifies the relative content and distribution of alloying elements in the alloy's microstructure, consequently impacting its microstructural characteristics.
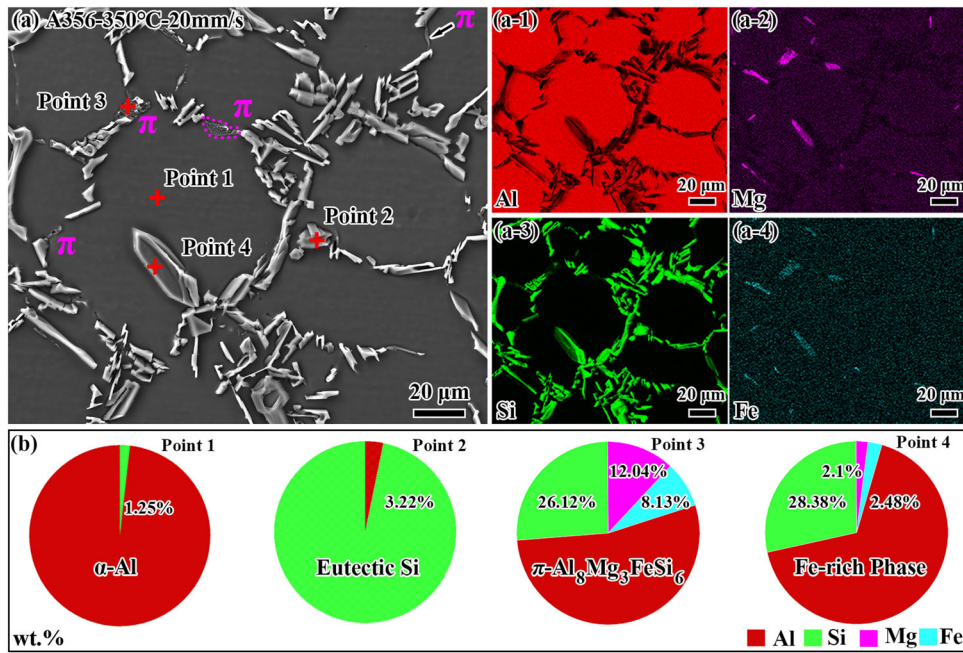
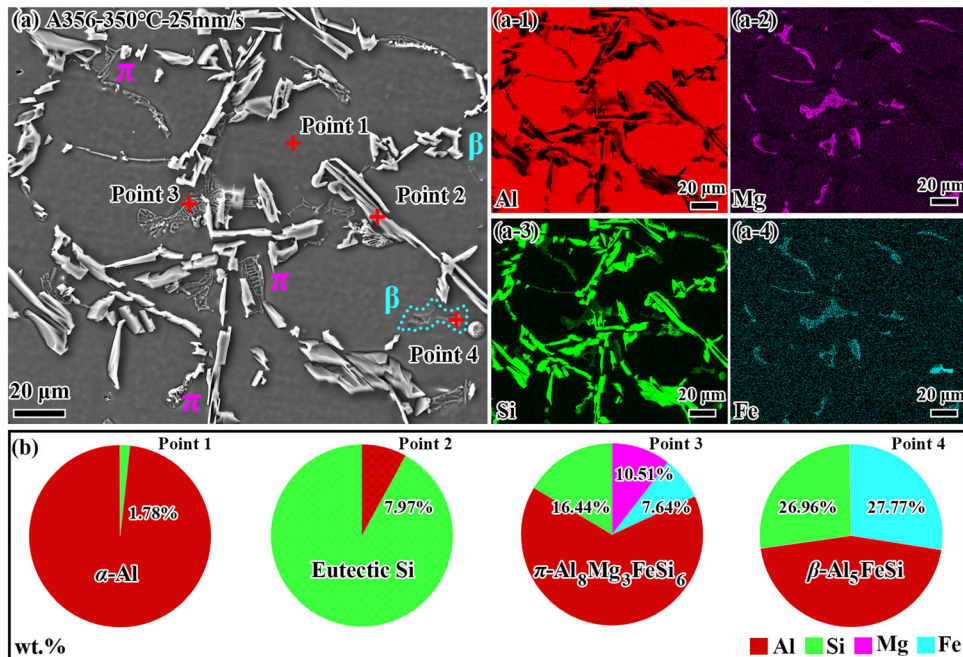Figure 15. (a) The ESEM image of A356-350-20 sample; (a-1)–(a-4) EDS mapping; (b) EDS results of Figure (a).

Figure 16. (a) The FESEM image of A356-350-25 sample; (a-1)–(a-4) EDS mapping; (b) EDS results of Figure (a).

Microstructure Evolution Mechanism

Semi-Solid Slurry Preparation Stage

The preparation technique proposed in this paper involves the induction of a semi-solid slurry through transient undercooling of the melt, which can achieve extremely high cooling rates for the A356 melt in a short period of time. The strong quenching effect results in explosive nucleation of the A356 alloy melt, leading to the rapid growth of primary α-Al phase in a spherical or nearly spherical.

Homogenization Stage

As shown in Figure 17b, serves to further reduce the fluctuation of solute concentration within the liquid phase, thereby mitigating to some extent the localized aggregation
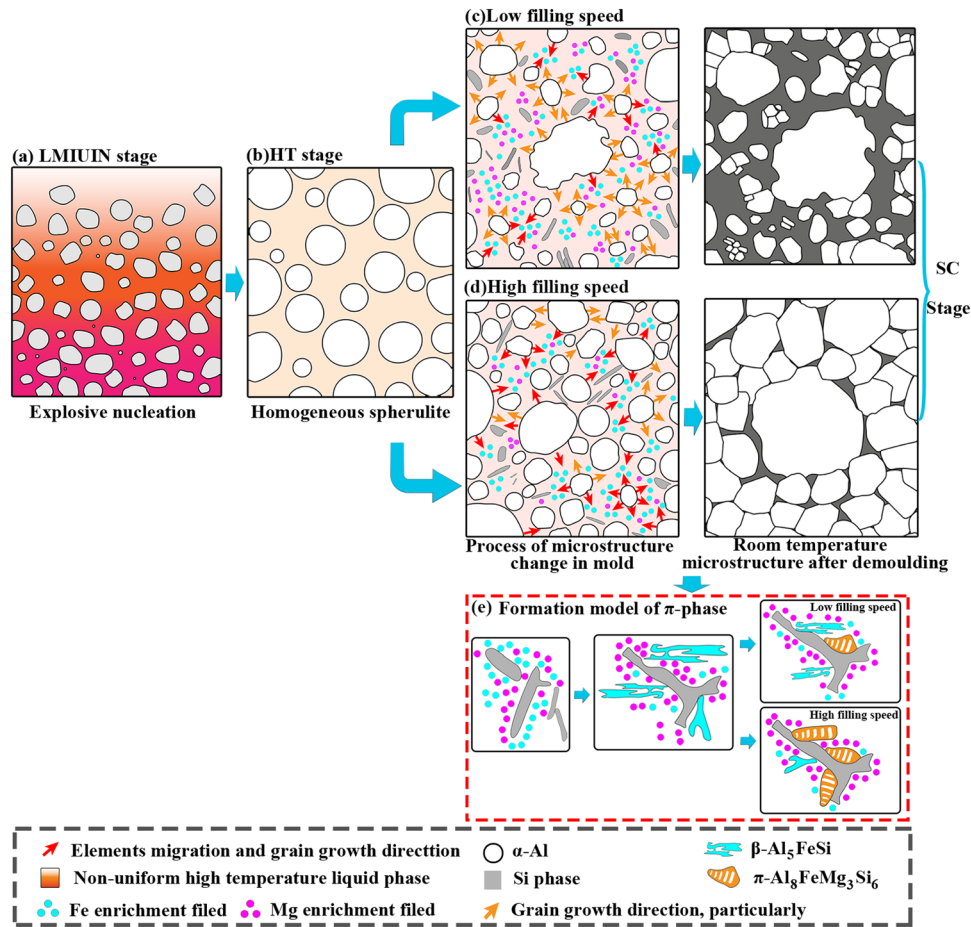
Figure 17. *Microstructure evolution diagram ofA356 alloy from semi-solid slurry preparation to rheological squeeze casting process.*

of solute elements (such as Si, Mg, Fe), thus achieving the homogenization of the microstructure.[37,38]

Rheological Squeeze Casting Stage

Secondary nucleation occurs between the remaining high-temperature liquid phase and the relatively lower temperature of the shot sleeve and/or the inner walls of the mold cavity. Furthermore, the remaining high-temperature liquid phase is undercooled, and the nuclei are preserved in the high-temperature residual liquid phase, thus having a high chance of growing during subsequent forming processes. As shown in Figure 17c, d, the A356 alloy in the rheological squeeze casting stage can be divided into the following two cases:

    (1)   Low mold temperature and low filling speed

In the filling process, due to the action of the punch, the melt induced by the transient undercooling nucleation stage with primary α_1-Al grains and residual liquid phase is pushed forward to enter the mold cavity. Subsequently, aluminum atoms precipitate from the residual undercooled

liquid phase near the α_1-Al grains and adhere to the primary α_1-Al grains, allowing the α_1-Al grains to grow. In addition, while the primary α_1-Al grains are growing, the residual liquid phase undergoes secondary nucleation and eutectic reaction inside the mold cavity, forming fine tree-like secondary α_2-Al phases.

The boundary layer solute distribution diagram and the composition undercooling diagram of the solid/liquid interface are presented in Figure 18. Figure 18a illustrates the expulsion of solute elements (Mg, Fe, Si, etc.) into the residual liquid phase during the growth of primary α_1-Al and secondary nucleated α_2-Al phases. As the temperature decreases, the concentration of solute elements in the next layer of solid phase that is pushed outward will be higher than in the previous layer. With the gradual increase in solute element content in the residual liquid phase, the solidification temperature is also lowered. Due to the low diffusion of Mg, Fe, and other elements in the solid phase, they generate undercooling in the composition at the solid/liquid interface, thus forming a stable solute-enriched layer at the interface. Moreover, combined with the results of numerical simulation and the statistical results of the
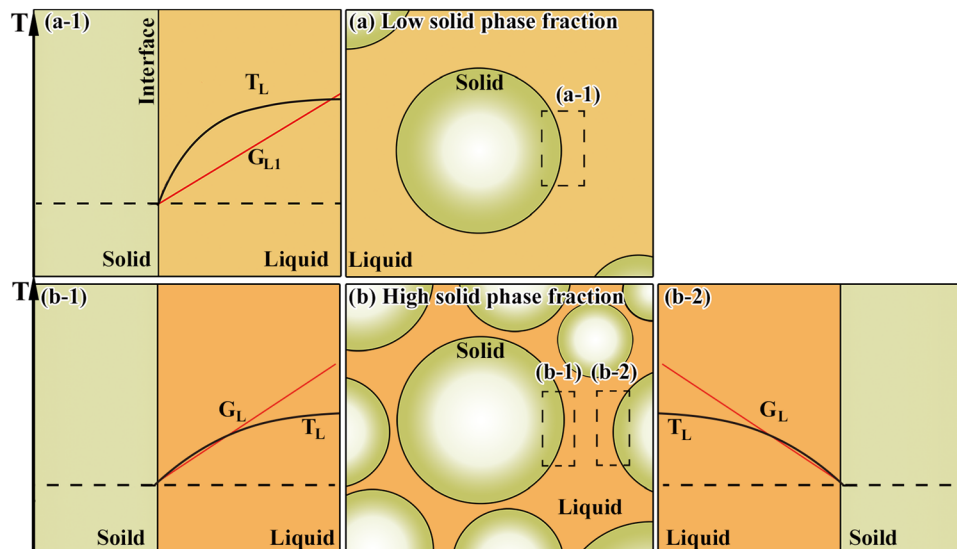
Figure 18. *Diagram of composition undercooling at solid/liquid interface front.*

volume fractions of each phase (refer to Figures 7, 8, 11, 12), it can be inferred that, because of the low mold temperature and filling speed, the high fraction of solid phase may likely lead to the mutual deforming compression of the primary α_1-Al grains under the punch pressure. This entanglement of some grains could lead to irregular grain shape, enhancing the likelihood of grain growth in a specific direction and making solute elements prone to accumulate along a specific orientation. This explains the occurrence of irregularly shaped grains alongside spherical and dendritic grains (as shown in Figures 11, 13).

In conjunction with the composition undercooling theory, if the solute atom expulsion rate at the interface is greater than the diffusion rate, as illustrated in Figures 17c and 18a, a-1, where G_L and G_{L1} depict the actual temperature gradient at the interface, and T_L represents the actual liquidus line temperature, the region where G_{L1} intersects with T_L is the composition undercooling zone. As the process of attachment growth, primary α_1-Al phase, and secondary nucleated grains (α_2-Al) continues, the concentration of solute elements in the residual undercooled liquid phase increases, leading to a further increase in the degree of composition undercooling. When the maximum value of the composition undercooling exceeds the amount of undercooling required for heterogeneous nucleation, a certain portion of homogeneous nucleation and growing α_2-Al equiaxed grains will appear in the residual liquid phase.

(2)   High mold temperature and high filling speed

Firstly, the elevation of the mold temperature and filling speed facilitates the rapid filling of the mold cavity by the molten metal and results in a slower cooling rate, enabling the semi-solid slurry within the cavity to solidify almost uniformly. The primary α_1-Al phase induced by transient undercooling of the melt and the secondary nucleated α_2-Al

phase both show a significant tendency to grow fully during rheological squeeze casting forming process. Additionally, demonstrated in Figures 17d and 18b, b-1, b-2, under the conditions of high mold temperature (350 °C) and high filling speed (20–25 mm/s), the eutectic structure has the lowest volume fraction, and the volume fraction of α-Al phase is the highest ($\sim 84.95\%$), indicating the potential for competitive growth between the secondary nucleated α_2-Al and primary α_1-Al phases during the growth process. When the volume fractions of the α-Al phase in the overall system increase to a certain range, the superposition effect of the temperature field between adjacent grains is further strengthened. As multiple adjacent grains simultaneously expel solute elements during the growth process, the superposition effect of the solute concentration field also strengthens (see Figure 18b–b-2). Additionally, higher mold temperature and faster filling speed are more conducive to reducing the actual temperature gradient at the solid/liquid interface. Thus, the nucleation sites within the entire system exist in a relatively uniform temperature and concentration environment and experience essentially the same solidification conditions. This fosters the experience of essentially identical solidification conditions. Consequently, the preferential growth mode of the grains within the system is significantly suppressed during the growth process, with the grains primarily growing in a relatively uniform spherical manner in all directions (as depicted in Figure 17d and Figure 18b–b-2).

The more significant finding of this study is that merely by controlling rheological squeeze casting process, the precipitation of intermetallic compounds in the microstructure can be achieved, specifically π-Al$_8$FeMg$_3$Si$_6$ and β-Al$_5$FeSi phases. This is evident from the EDS results at points 3 and 4, as shown in Figures 13, 15, and 17e. The

results indicate a tendency for the π-$Al_8FeMg_3Si_6$ phase and β-Al_5FeSi phase to be combined. Combining the aforementioned analysis, it is found that the structure, content, and morphology of the Fe-rich phase are not only related to the degree of Fe accumulation but also to the non-equilibrium solidification process.[21] On the one hand, during the solidification process, the higher filling speed conditions (20 mm/s) make it easier for the β-Al_5FeSi phase to form and grow fully. Additionally, the enrichment of Mg around the β-Al_5FeSi phase and eutectic Si provides conditions for the formation of the π-$Al_8FeMg_3Si_6$ phase within the high Mg concentration zone. On the other hand, it is evident from Figure 16 that under these processing conditions, the β-Al_5FeSi phase is likely to fully transform into the π-$Al_8FeMg_3Si_6$ phase. However, if the filling speed is further increased, excessively high filling speed is not conducive to maintaining good solid/liquid flow coordination in the A356 alloy melt during the filling process, leading to a disruption of the stability of the entire filling process. This results in the aggregation of solute elements along specific orientations, which is detrimental to the complete decomposition of the β-Al_5FeSi phase. Due to the insufficient growth of the β-Al_5FeSi phase, the Mg concentration in the adjacent melt is not sufficient to form the π-$Al_8FeMg_3Si_6$ phase. Consequently, in the room temperature condition both π-$Al_8FeMg_3Si_6$ phase and the yet-to-be decomposed β-Al_5FeSi phase can be observed.

Conclusions

1. In the rheological squeeze casting process of A356 alloy, an investigation of the temperature field, velocity field, and solid-phase fraction evolution revealed that a combination of high mold temperatures (505–525 °C) and high filling speeds (20–22 mm/s) improves the stability of the semi-solid slurry filling in the mold cavity and the uniformity of the internal temperature distribution, thereby effectively reducing the temperature gradient within the slurry.
2. The influence of process parameters on maximum temperature difference (°C) within the casting follows the sequence: mold temperature > filling speed, whereas the high solid-phase fraction melt (Fs = 60–100%) follows the sequence: filling speed > mold temperature. The optimal process parameter combination is a filling speed of 20 mm/s and a mold temperature of 350 °C.
3. Casting structures exhibited poor uniformity when the filling speed was 10–15 mm/s and the mold temperature was 200–300 °C. This led to a microstructure consisting of nearly spherical primary α_1-Al grains, fine dendritic secondary α_2-Al grains, and a high density of eutectic clusters. However, with increased filling speed and mold temperature (20–25 mm/s and 300–350 °C, respectively), the average equivalent diameter of the α-Al phase increased to 39.48–44.27 μm with a significant improvement in the eutectic clusters, and the eutectic Si was uniformly distributed in the form of long rod-shaped or block-shaped structures.
4. A mold temperature of 350 °C and a filling speed of 20 mm/s resulted in the Fe-rich intermetallic compound primarily composed of the π-$Al_8FeMg_3Si_6$ phase. However, when the filling velocity increased to 25 mm/s, both the β-Al_5FeSi phase and the π-$Al_8FeMg_3Si_6$ phase were present. Simultaneously, the microstructure of the Fe-rich intermetallic compound gradually changed from script-like to needle-like.
5. The A356 alloy with different microstructure morphology characteristics exhibits different mechanisms for forming semi-solid microstructures: (1) Under low mold temperature and low filling speed conditions, it is mainly affected by component undercooling. When the maximum value of the component undercooling is greater than the undercooling required for a large amount of heterogeneous nucleation, a portion of homogeneous nucleation and growth of α_2-Al grains will occur in the residual liquid phase. (2) Under high mold temperature and high filling speed conditions, the nucleation in the entire system exists in a relatively uniform temperature field and solute field growth environment, and has basically the same solidification conditions. The preferred growth mode of the grains in the system is strongly inhibited during the growth process, and they can only grow in a relatively uniform spherical manner in all directions.

Funding

REFERENCES

1. R. Koeune, J.P. Ponthot, A one phase thermomechanical model for the numerical simulation of semi-solid material behaviour. application to thixoforming. Int. J. Plast. **58**, 120–153 (2014). https://doi.org/10.1016/j.ijplas.2014.01.004
2. W. Yu, H. He, W. Zhang et al., Modulation of the natural aging effect on subsequent artificial aging in Al–Mg–Si aluminum alloys with alloying content ∼ 1 wt% through temperature tuning. J. Alloy. Compd. **814**, 152277 (2020). https://doi.org/10.1016/j.jallcom.2019.152277

3. H. Ding, Z. Tao, S. Liu et al., A high-performing sulfur-tolerant and redox-stable layered perovskite anode for direct hydrocarbon solid oxide fuel cells. Sci. Rep. **5**, 18129 (2015). https://doi.org/10.1038/srep18129

4. D. Teng, G. Zhang, S. Zhang et al., Response of mechanical properties of A356 alloy to continuous rheological extrusion Al–5Ti–0.6C–xCe alloy addition upon different Ce contents. J. Mater. Res. Technol-JMRT **27**, 209–224 (2023). https://doi.org/10.1016/j.jmrt.2023.09.203

5. M.C. Flemings, Behavior of metal alloys in the semisolid state. Metall. Mater. Trans. B-Proc. Metall. Mater. Proc. Sci. **22**, 957–981 (1991)

6. A. Megalingam, A.H.B. Ahmad, M.R.B. Maarof et al., Viscosity measurements in semi-solid metal processing: current status and recent developments. Int. J. Adv. Manuf. Technol. **119**, 1435–1459 (2022). https://doi.org/10.1007/s00170-021-08356-w

7. W.J. Gao, S.M. Xing, G.Y. Yan et al., Effect of oscillation frequency on microstructure of A356 slurry prepared by semi-solid metal forming with flow. J. Mater. Process. Technol. (2023). https://doi.org/10.1016/j.jmatprotec.2022.117829

8. R. Haghayeghi, E.J. Zoqui, A. Halvaee et al., An investigation on semi-solid Al–7Si–0.3 Mg alloy produced by mechanical stirring. J. Mater. Process. Technol. **169**, 382–387 (2005). https://doi.org/10.1016/j.jmatprotec.2005.04.071

9. G. Zhu, J. Xu, Z. Zhang et al., Annular electromagnetic stirring—a new method for the production of semi-solid A357 aluminum alloy slurry. Acta Metall. Sin.—Engl. Lett. **22**, 408–414 (2009). https://doi.org/10.1016/S1006-7191(08)60116-7

10. D.K. Yadav, I. Chakrabarty, Effect of cooling slope casting and partial remelting treatment on microstructure and mechanical properties of A319–xMg$_2$Si In-Situ composites. Mater. Sci. Eng. A-Struct. Mater. Prop. Microstruct. Process. (2020). https://doi.org/10.1016/j.msea.2020.139790

11. W.T. Xiong, R.F. Zhou, Z.X. Liu et al., Effects of Forming specific pressure and filling speed on microstructure and mechanical properties of thin-walled cusn10p1 alloy parts by rheological squeeze forming. Int. J. Met. **18**, 1438–1454 (2024). https://doi.org/10.1007/s40962-023-01109-3

12. B. Zhou, Y.-L. Kang, G.-M. Zhu et al., Forced convection rheoforming process for preparation of 7075 aluminum alloy semisolid slurry and its numerical simulation. Trans. Nonferrous Met. Soc. China **24**, 1109–1116 (2014). https://doi.org/10.1016/S1003-6326(14)63169-1

13. M.M. Shehata, S. El-Hadad, M.E. Moussa et al., The combined effect of cooling slope plate casting and mold vibration on microstructure, hardness and wear behavior of Al–Si alloy (A390). Int. J. Met. **15**, 763–779 (2021). https://doi.org/10.1007/s40962-020-00497-0

14. G. Li, W.-Y. Qu, M. Luo et al., Semi-solid processing of aluminum and magnesium alloys: status, opportunity, and challenge in China. Trans. Nonferrous Met. Soc. China **31**, 3255–3280 (2021). https://doi.org/10.1016/S1003-6326(21)65729-1

15. S.Y. Ren, F. Wang, J. Sun et al., Gating system design based on numerical simulation and production experiment verification of aluminum alloy bracket fabricated by semi-solid rheo-die casting process. Int. J. Met. **16**, 878–893 (2022). https://doi.org/10.1007/s40962-021-00648-x

16. P. Das, B. Bhuniya, S.K. Samanta et al., Studies on die filling of A356 Al alloy and development of a steering knuckle component using rheo pressure die casting system. J. Mater. Process. Technol. **271**, 293–311 (2019). https://doi.org/10.1016/j.jmatprotec.2019.04.014

17. K. Chanyathunyaroj, U. Patakham, S. Kou et al., Microstructural evolution of iron-rich intermetallic compounds in scandium modified Al–7Si–0.3 Mg alloys. J. Alloy. Compd. **692**, 865–875 (2017). https://doi.org/10.1016/j.jallcom.2016.09.132

18. L. Sweet, S.M. Zhu, S.X. Gao et al., The effect of iron content on the iron-containing intermetallic phases in a cast 6060 aluminum alloy. Metall. Mater. Trans. A-Phys. Metall. Mater. Sci. **42**, 1737–1749 (2011). https://doi.org/10.1007/s11661-010-0595-6

19. J.A. Taylor, Iron-containing intermetallic phases in Al–Si based casting alloys. Procedia Mater. Sci. **1**, 19–33 (2012). https://doi.org/10.1016/j.mspro.2012.06.004

20. O. Elsebaie, A.M. Samuel, F.H. Samuel, Effects of Sr-modification, iron-based intermetallics and aging treatment on the impact toughness of 356 Al–Si–Mg alloy. J. Mater. Sci. **46**, 3027–3045 (2011). https://doi.org/10.1007/s10853-010-5181-1

21. J.H. Zhao, Y. Guo, B. Xu et al., Effect of microstructure evolution of iron-rich intermetallic compounds on mechanical property of Al–7Si–0.3 Mg casting alloy with low iron content. Metall. Mater. Trans. B-Proc. Metall. Mater. Proc. Sci. **53**, 548–560 (2022). https://doi.org/10.1007/s11663-021-02390-5

22. A. Gorny, J. Manickaraj, Z. Cai et al., Evolution of Fe based intermetallic phases in Al–Si hypoeutectic casting alloys: Influence of the Si and Fe concentrations, and solidification rate. J. Alloy. Compd. **577**, 103–124 (2013). https://doi.org/10.1016/j.jallcom.2013.04.139

23. Z. Li, H. Yan, Modification of primary α-Al, eutectic silicon and β-Al$_5$FeSi phases in as-cast AlSi$_{10}$Cu$_3$ alloys with (La+Yb) addition. J. Rare Earths **33**, 995–1003 (2015). https://doi.org/10.1016/S1002-0721(14)60517-2

24. G.-C. Gu, L.-X. Xiang, R.-F. Li et al., Microstructure, segregation and mechanical properties of A356 alloy components fabricated by rheo-HPDC combined with the swirled enthalpy equilibration device (SEED)

process. J. Mater. Res. Technol-JMRT **26**, 7803–7815 (2023). https://doi.org/10.1016/j.jmrt.2023.09.153

25. A.M. Samuel, Y. Zedan, H.W. Doty et al., Role of the addition of la and ce on the cooling characteristics and porosity formation in A356 and A413 Alloys. Int. J. Met. **16**, 553–572 (2022). https://doi.org/10.1007/s40962-021-00613-8

26. C. Narducci Jr., G.L. Brollo, R.H.M. De Siqueira et al., Effect of Nb addition on the size and morphology of the β-Fe precipitates in recycled Al–Si alloys. Sci. Rep. **11**, 9613 (2021). https://doi.org/10.1038/s41598-021-89050-5

27. R. Qin, R.F. Yan, Z.P. Guan et al., Effect of vanadium on Fe-rich phase, mechanical properties and thermal conductivity of hypoeutectic Al–Si alloy. Mater. Res. Express (2021). https://doi.org/10.1088/2053-1591/abe5f0

28. Z. Ma, H. Zhang, X. Zhang et al., Rheological behaviour of partially solidified A356 alloy: experimental study and constitutive modelling. J. Alloy. Compd. **803**, 1141–1154 (2019). https://doi.org/10.1016/j.jallcom.2019.06.345

29. M. Madanat, M. Liu, J. Banhart, Reversion of natural ageing in Al–Mg–Si alloys. Acta Mater. **159**, 163–172 (2018). https://doi.org/10.1016/j.actamat.2018.07.066

30. J.F. Hao, B. Chen, P. Xia et al., Effect of solid solution treatment on microstructure and mechanical properties of Al–Si–Cu–Mg alloy prepared by semi-solid squeeze casting. Int. J. Met. (2023). https://doi.org/10.1007/s40962-023-01160-0

31. A. Kumbhare, P. Biswas, A. Bisen et al., Investigation of effect of the rheological parameters on the flow behavior of ADC12 Al alloy in rheo-pressure die-casting. Int. J. Met. **17**, 2836–2848 (2023). https://doi.org/10.1007/s40962-023-00962-6

32. P. Das, S.K. Samanta, P. Dutta, Rheological behavior of Al–7Si–0.3Mg alloy at Mushy State. Metall. Mater. Trans. B-Proc. Metall. Mater. Proc. Sci. **46**, 1302–1313 (2015). https://doi.org/10.1007/s11663-015-0290-5

33. M. Grujicic, G. Cao, R.S. Miller, Computer modeling of the evolution of dendrite microstructure in binary alloys during non-isothermal solidification. J. Mater. Synth. Process. **10**, 191–203 (2002). https://doi.org/10.1023/A:1023022214920

34. J.A. Spittle, S.G.R. Brown, Computer simulation of the effects of alloy variables on the grain structures of castings. Acta Metall. **37**, 1803–1810 (1989)

35. W.T. Xiong, R.F. Zhou, Z.X. Liu et al., Effects of melt-constrained flow-induced nucleation channel length on temperature field and microstructure of $CuSn_{10}P_1$ alloy semi-solid slurry. Int. J. Met. **17**, 1926–1947 (2023). https://doi.org/10.1007/s40962-022-00877-8

36. L.L. Fan, M.Y. Zhou, Y.W.X. Zhang et al., The semi-solid microstructural evolution and coarsening kinetics of AZ80-0.2Y-0.15Ca magnesium alloy. Mater Charact **154**, 116–126 (2019). https://doi.org/10.1016/j.matchar.2019.05.019

37. S.M. So, K.Y. Kim, S.J. Lee et al., Effects of Sn content and hot deformation on microstructure and mechanical properties of binary high Sn content Cu–Sn alloys. Mater. Sci. Eng. A-Struct. Mater. Prop. Microstruct. Process. (2020). https://doi.org/10.1016/j.msea.2020.140054

38. P. Das, P. Dutta, Phase field modelling of microstructure evolution and ripening driven grain growth during cooling slope processing of A356 Al alloy. Comput. Mater. Sci. **125**, 8–19 (2016). https://doi.org/10.1016/j.commatsci.2016.08.022